Inorganic Chemistry

Article

pubs.acs.org/IC

[1,2,4]Triazolo[4,3-*a*]Pyridines as Bridging Ligands—Magnetism of Azole-Bridged Dinuclear Copper(II) Complexes Influenced by the Trigonal Distortion Parameter τ

Dominic Kaase,[†] Carla Gotzmann,[†] Stephan Rein,[‡] Yanhua Lan,[§] Sylwia Kacprzak,*[,‡] and Julia Klingele*[,†]

[†]Institut für Anorganische und Analytische Chemie, Albert-Ludwigs-Universität Freiburg, Albertstr. 21, D-79104 Freiburg, Germany

[‡]Institut für Physikalische Chemie, Albert-Ludwigs-Universität Freiburg, Albertstr. 21, D-79104 Freiburg, Germany

[§]Institut für Anorganische Chemie, Karlsruher Institut für Technologie (KIT), Engesserstr. 15, Geb. 30.45, D-76131 Karlsruhe, Germany

Supporting Information

ABSTRACT: The dinuclear doubly azole-bridged copper(II) complexes $[Cu^{II}_2(\mathbf{L})_2(MeCN)_4](ClO_4)_4 \cdot 3.73MeCN \cdot 0.80H_2O$ and $[Cu^{II}_2(\mathbf{L})_6](ClO_4)_4 \cdot$solvent (solvent = $2MeCN \cdot H_2O$; $2MeCN \cdot 2H_2O$; $1.5MeOH \cdot 3.5H_2O$) were prepared [**L** = 3-(6-methyl-2-pyridyl)-[1,2,4]triazolo[4,3-*a*]pyridine]. Structural characterizations revealed very different local geometries about the copper(II) ions, being trigonal bipyramidal for the former (τ = 0.76) and square pyramidal for the latter (τ = 0.07, 0.15, 0.07) complex. Magnetic measurements of bulk material $[Cu^{II}_2(\mathbf{L})_2(H_2O)_4](ClO_4)_4$ and $[Cu^{II}_2(\mathbf{L})_6](ClO_4)_4 \cdot 2H_2O$ revealed antiferromagnetic coupling in both complexes, however, of very different strengths. Electron paramagnetic resonance (EPR) spectroscopy was applied to investigate magnetic properties of the complexes in detail. These experimental findings were supported by broken-symmetry DFT calculations. Systematic magneto-structural correlations are discussed.

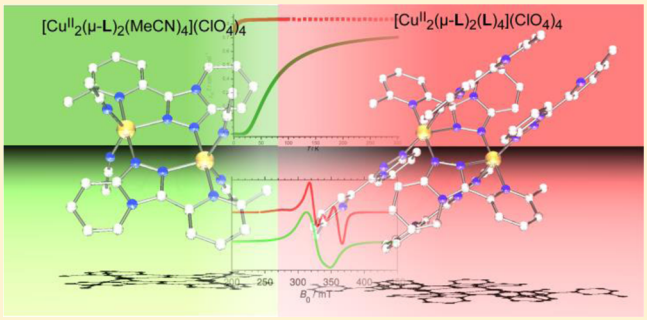

INTRODUCTION

In 3-position substituted [1,2,4]triazolo[4,3-*a*]pyridines consist of a 1,2,4-triazole ring, fused *via* N^4 and C^5 to a benzene ring and substituted at the remaining carbon atom. Those ligands are able to form dinuclear complexes, bridging two metal centers *via* N^1 and N^2 of the diazine unit of their triazolopyridine core. Dinuclear copper(II) complexes containing such a diazine unit are especially interesting for investigation of their magneto-structural correlations.[1,2] In such azole-bridged complexes usually antiferromagnetic coupling is observed, the strength depending on the geometry of the Cu−(N═N)$_2$−Cu bridging unit.[1] The more symmetric the bridging mode the better the overlap between the orbitals and stronger the magnetic coupling. A similar dependence on the metal···metal bridge has been observed for dinuclear oxido-bridged copper(II) complexes. Increase of both the Cu−Cu distance and the Cu−O−Cu angle resulted in decrease of the magnetic coupling constant *J*.[3] Dinuclear copper(II) complexes with doubly azole-bridged metal ions have been previously observed with the anionic ligands 3-amino-5-(2-pyridyl)-pyrazolate (**A**),[4] 3-(2-pyridyl)pyrazolate (**B**),[5−7] 3-(6-methyl-2-pyridyl)pyrazolate (**C**),[8] with the 1,2,4-triazole-based ligands **D**,[9] **E**,[1,10] **F**,[11] and **G**,[12] as well as with the ligand 6-methyl-3-pyridin-2-yl-7*H*-[1,2,4]triazolo[3,4-*b*][1,3,4]thiadiazine (**H**) (Figure 1a).[9] Also, 3,5-di(2-pyridyl)-pyrazolate (**I**, Figure 1a) is known to form dinuclear complexes of that type.[13−15] These complexes, where analyzed, feature antiferromagnetic couplings of different strengths, ranging from $J = -31$ cm^{-1} for $[Cu^{II}_2(\mathbf{F})_2Cl_4]$[11] to $J = -368$ cm^{-1} for $[Cu^{II}_2(\mathbf{I})_2(H_2O)_2](ClO_4)_2$.[15] Apart from $[Cu^{II}_2(\mathbf{F})_2Cl_4]$,[11] where the coordination environment about the copper(II) ions is best described as trigonal bipyramidal (τ = 0.68−0.71), those complexes feature a square pyramidal coordination with the $d_{x^2-y^2}$ orbitals being parallel to each other and pointing directly to the N atoms of the azole bridge. Here we report on the synthesis of two new doubly azole-bridged dinuclear copper(II) complexes with similar Cu−(N═N)$_2$−Cu units but fundamental different magnetic behavior compared to each other and to the compounds mentioned above. Studying the coordination geometries of these complexes in detail, we will show that, for the magnetic coupling strength, even more important than the symmetry of the Cu−(N═N)$_2$−Cu unit is the degree of trigonality τ[16] of the coordination sphere and the orientation of the resulting magnetic orbitals relative to the bridging plane.

Recently, we reported on the complexation behavior of the 3-(2-pyridyl)- and the 3-(2-pyrazyl)-substituted derivatives of [1,2,4]triazolo[4,3-*a*]pyridine.[17,18] Both ligands [$\mathbf{L^1}$: 3-(2-pyridyl)-[1,2,4]triazolo[4,3-*a*]pyridine,[17] $\mathbf{L^2}$: 3-(2-pyrazyl)-[1,2,4]triazolo[4,3-*a*]pyridine,[18] Figure 1b] have been found

Received: January 30, 2014
Published: May 16, 2014

   dx.doi.org/10.1021/ic500226z | *Inorg. Chem.* 2014, 53, 5546−5555

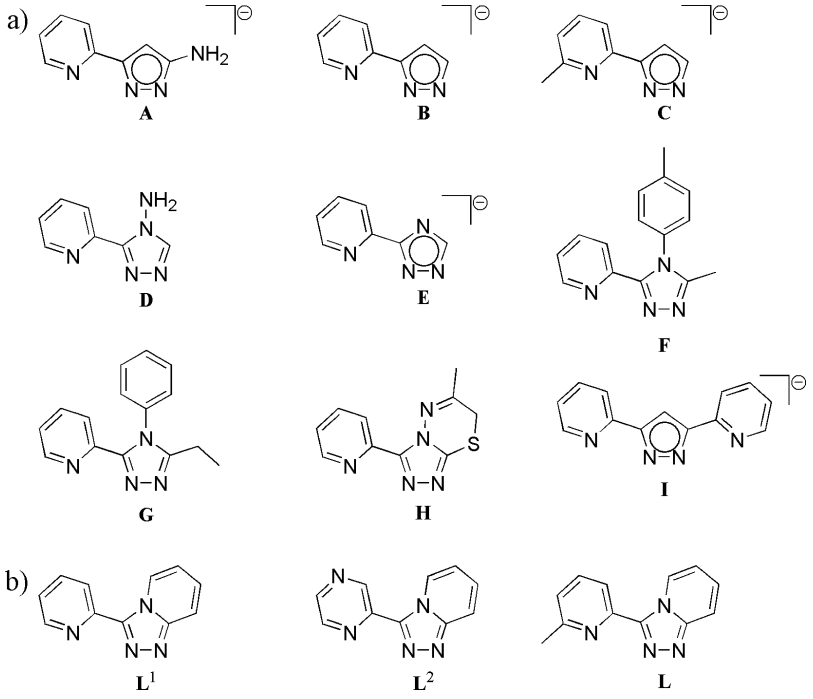

Figure 1. (a) Ligands forming dinuclear copper(II) complexes with doubly azole-bridged metal ions found in literature;[4−15] (b) the 3-substituted [1,2,4]triazolo[4,3-*a*]pyridines $\mathbf{L^1}$, $\mathbf{L^2}$, and **L**.

Scheme 1. Synthesis of the Mononuclear 2:1-Type Complexes $[Cu^{II}(L^1)_2(ClO_4)_2]$ and $[Cu^{II}(L^1)_2(MeOH)_2](ClO_4)_2$[17] and the 2D Polymeric Complex $[Cu^{II}(L^2)_2](ClO_4)_2$.[18]

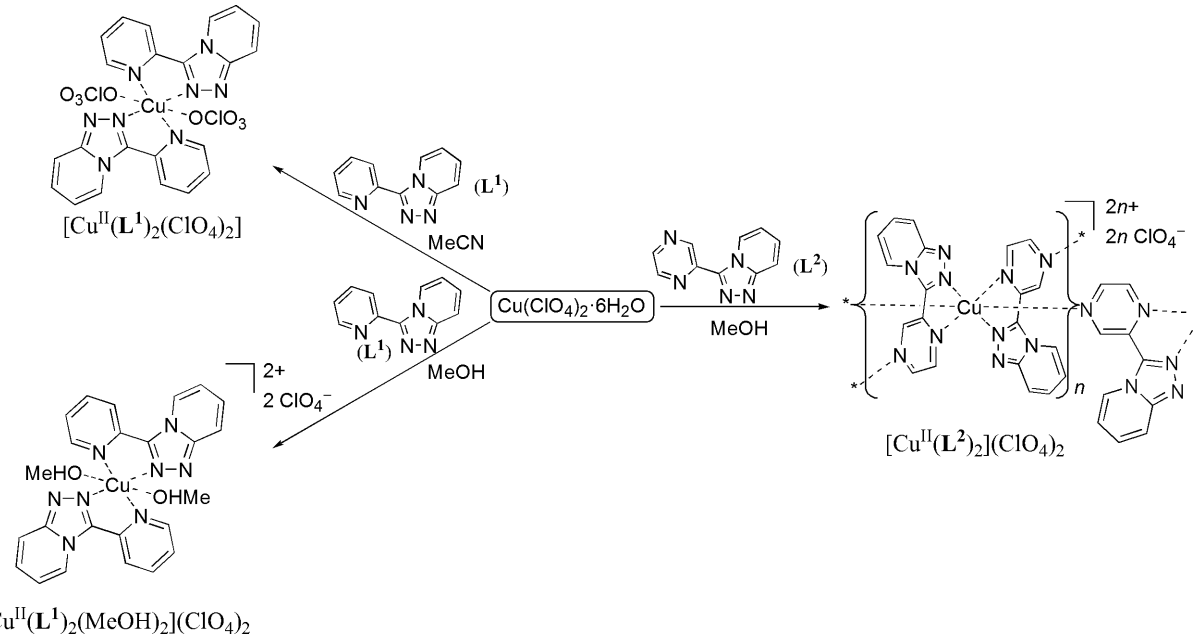

to readily coordinate 3d transition metal ions. With $Cu(ClO_4)_2 \cdot 6H_2O$, $\mathbf{L^1}$ forms mononuclear complexes with a 2:1 ligand-to-metal ion stoichiometry and *trans* coordinated coligands,[17] whereas $\mathbf{L^2}$ forms a two-dimensional (2D) network of $[Cu^{II}(\mathbf{L^2})_2]^{2+}$ cores that are connected via the pyrazyl group of the ligand's substituent (Scheme 1).[18] Apparently neither $\mathbf{L^1}$ nor $\mathbf{L^2}$ tends to act as a bridging ligand using its diazine unit. Here, investigations on the coordination behavior of 3-(6-methyl-2-pyridyl)-[1,2,4]triazolo[4,3-*a*]pyridine (**L**, Figure 1b), a derivative of $\mathbf{L^1}$ featuring an additional methyl group in the 6-position of the pyridine substituent, are presented. This feature is expected to impose sterical stress on the coordination sphere of the resulting transition metal complexes and therefore hinder the formation of 2:1-type complexes with a *trans*-$(N',N^1)_2$ coordination, like the ones $\mathbf{L^1}$[17] and other similar 2-pyridyl-substituted azole-ligands[18−24] tend to form.

RESULTS AND DISCUSSION

Ligand Synthesis and Structural Characterization. Analogously to the preparation of $\mathbf{L^1}$[17] and $\mathbf{L^2}$,[18] the ligand **L** was formed from amidrazone *N*-(2-pyridylamino)-2-(6-

dx.doi.org/10.1021/ic500226z | Inorg. Chem. 2014, 53, 5546−5555

Scheme 2. Preparation of 3-(6-Methyl-2-pyridyl)-[1,2,4]triazolo[4,3-*a*]pyridine (L) from *N*-(2-pyridylamino)-2-(6-methylpyridine)amidine (J)

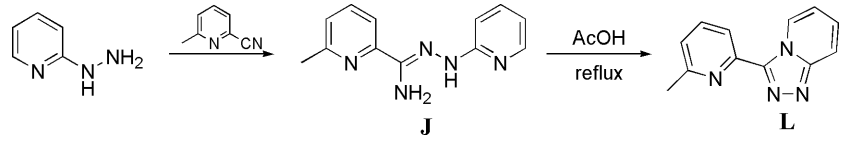

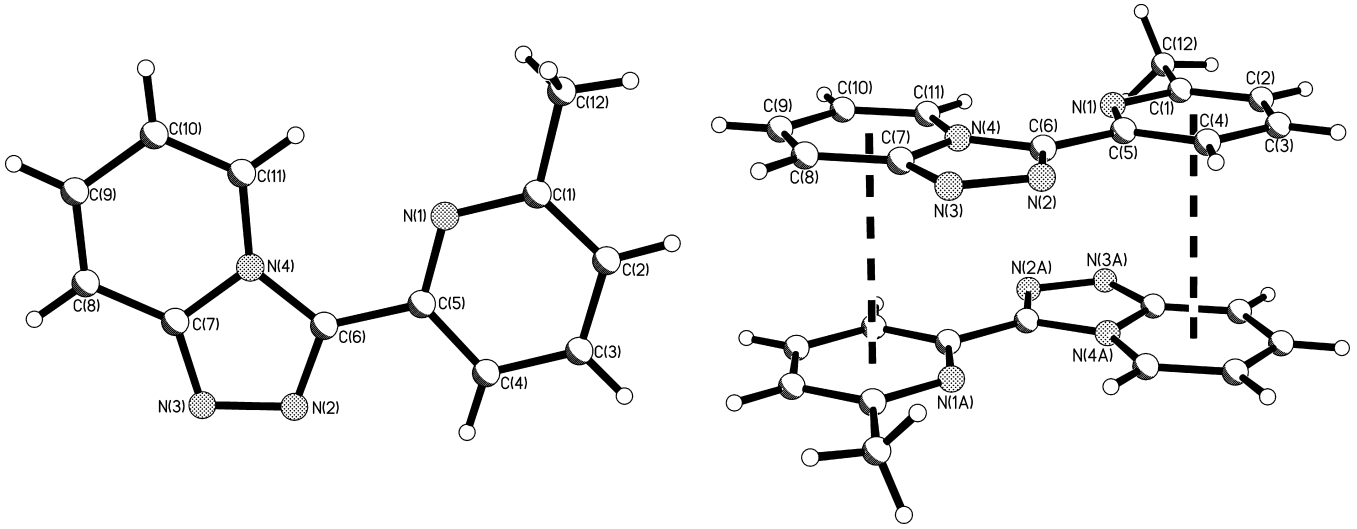

Figure 2. (left) View of the molecular structure of 3-(6-methyl-2-pyridyl)-[1,2,4]triazolo[4,3-*a*]pyridine (**L**); (right) $\pi-\pi$ stacking in the crystal structure of **L**. Selected distances [Å]: cent ⟨N(1)/C(1)/C(2)/C(3)/C(4)/C(5)⟩···cent ⟨C(7A)/C(8A)/C(9A)/C(10A)/C(11A)/N(4A)⟩ 3.527. Symmetry operation used to generate equivalent atoms: (A) $-x + 2, -y + 1, -z$.

Scheme 3. Reaction of L with $Cu(ClO_4)_2 \cdot 6H_2O$[a]

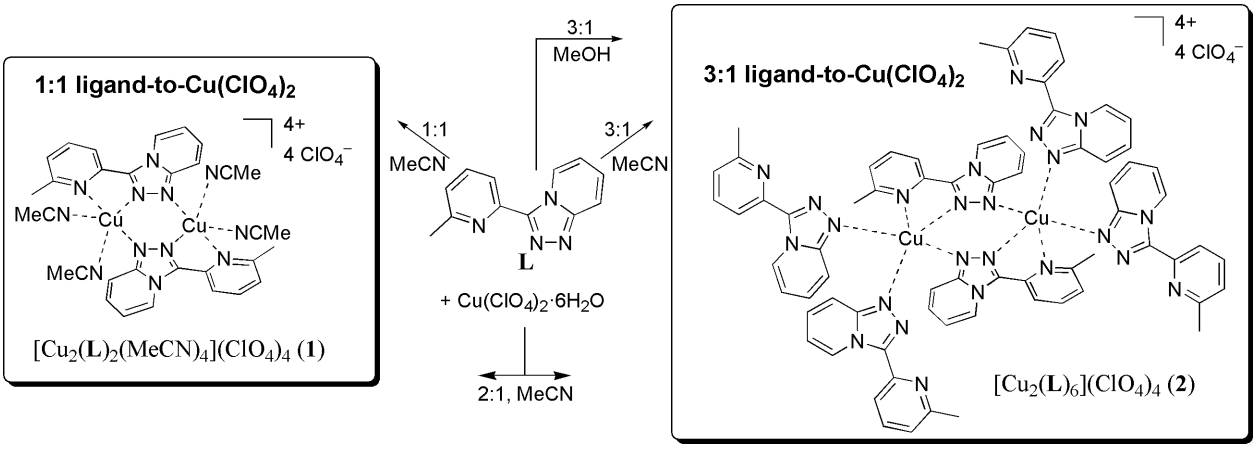

[a]Schematic drawing of the dinuclear complexes $[Cu^{II}_2(\mathbf{L})_2(MeCN)_4](ClO_4)_4$ (**1**) and $[Cu^{II}_2(\mathbf{L})_6](ClO_4)_4$ (**2**).

methylpyridine)amidine (**J**) (Scheme 2) on refluxing in acetic acid and was obtained in the form of a crystalline solid (Figure 2). Amidrazone **J** was prepared from 2-pyridylhydrazine under solvent-free conditions by the addition of 6-methyl-2-cyanopyridine, keeping the molten mixture at 80−85 °C for 7 d. Already in this step, **L** was formed as a byproduct in about 25−40% and could not be separated from amidrazone **J**. Attempts of recrystallization consequently resulted in mixtures of **J** and **L**; therefore, a crystalline mixture with about 25% of **L** was used as such for the preparation of pure **L**.

Differently from $\mathbf{L}^1$ [17] and $\mathbf{L}^2$,[18] where $\pi-\pi$ stacking is observed between the substituent of the triazole ring (2-pyridyl in $\mathbf{L}^1$ and 2-pyrazyl in $\mathbf{L}^2$) and the triazole ring of a neighboring molecule, in **L** stacking is observed between the 2-pyridyl substituent and the pyridine ring of the triazolopyridine unit of a neighboring molecule (Figure 2). The centroid−centroid distance is 3.527 Å, with offset angles of 16.5 and 15.8° to the former and latter ring, respectively.

Synthesis and Structural Characterization of Copper(II) Complexes. Copper(II) complexes of **L** were obtained from MeCN solutions by vapor diffusion of either Et_2O or TBME (TBME = *tert*-butyl methyl ether = 2-methoxy-2-methylpropane) into the reaction mixtures. The green complex $[Cu^{II}_2(\mathbf{L})_2(MeCN)_4](ClO_4)_4 \cdot 3.73MeCN \cdot 0.80H_2O$ (**1**·3.73MeCN·0.80H_2O) (Scheme 3 and Figure 3) was formed, when the appropriate 1:1 molar stoichiometry of ligand-to-

dx.doi.org/10.1021/ic500226z | *Inorg. Chem.* 2014, 53, 5546−5555

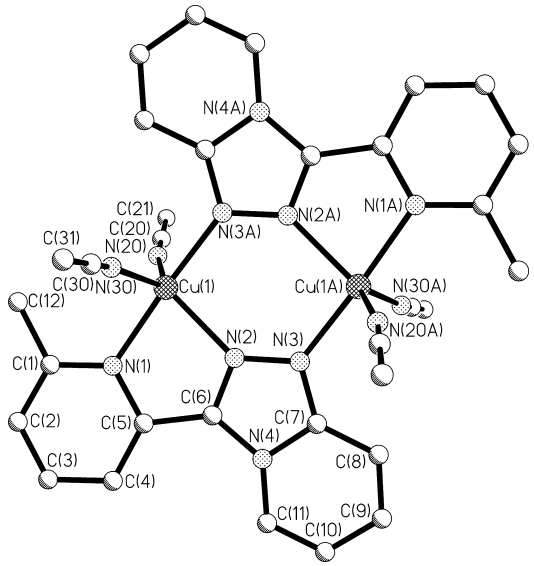

Figure 3. View of the molecular structure of $[Cu^{II}_2(\mathbf{L})_2(MeCN)_4]^{4+}$, the complex cation of **1**·3.73MeCN·0.80H_2O. Hydrogen atoms are omitted for clarity. Symmetry operation used to generate equivalent atoms: (A) $-x + 1, -y + 1, -z + 1$.

metal salt was used. Bulk material of this compound was obtained by drying the isolated crystalline material in air and was formulated as $[Cu^{II}_2(\mathbf{L})_2(H_2O)_4](ClO_4)_4$ (**1a**), according to elemental analysis.

When increasing the ligand concentration to a 2:1 molar stoichiometry of ligand-to-metal ion a mixture of the green compound **1**·3.73MeCN·0.80H_2O along with the red compound $[Cu^{II}_2(\mathbf{L})_6](ClO_4)_4$·2MeCN·$H_2O$ (**2**·2MeCN·H_2O, Scheme 3) was obtained. Only when the appropriate 3:1 molar ratio of ligand-to-metal salt was used, the red compound **2** could be obtained as the sole product. When using TBME for vapor diffusion into the MeCN solution compound **2**·2MeCN·2H_2O (Figure 4) was obtained. The use of Et_2O resulted in the formation of **2**·2MeCN·H_2O. After drying *in vacuo* **2**·2H_2O was obtained from both samples as bulk material.

From MeOH solution a green-brown precipitate with a 3:1 ligand-to-metal ion stoichiometry was isolated by addition of the appropriate amount of $Cu(ClO_4)_2$·6H_2O to a ligand solution. Single crystals suitable for X-ray diffraction of $[Cu^{II}_2(\mathbf{L})_6](ClO_4)_4$·1.5MeOH·3.5$H_2O$ (**2**·1.5MeOH·3.5H_2O) could be obtained from diluted MeOH solution (∼5 mM) after leaving the mixture for slow evaporation of the solvent in air. After drying the crystalline compound *in vacuo* **2**·2H_2O was obtained as bulk material. A 2:1 type copper(II) complex of **L** could not be prepared, neither from MeCN nor from MeOH. Neither could be prepared complexes of iron(II), cobalt(II), or nickel(II).

The coordination spheres about the copper(II) ions in **1**·3.73MeCN·0.80H_2O and **2**·solvent (solvent = 2MeCN·2H_2O; 2MeCN·H_2O; 1.5MeOH·3.5H_2O) are built by two ligands **L** coordinating with a (N',N^1,N^2)-double bridging motif.[20] The 5-fold coordination spheres of the copper(II) ions are completed by acetonitrile coligands and $N_{tp}{}^2$-coordinated ligands **L**, respectively. In $[Cu^{II}_2(\mathbf{L})_6](ClO_4)_4$·solvent (**2**·solvent), therefore, two different coordination modes are observed for **L**, and the complex cation is best formulated as $[(\mathbf{L})_2Cu^{II}(\mu\text{-}\mathbf{L})_2Cu^{II}(\mathbf{L})_2]^{4+}$. The ligand coordinates either solely *via* $N_{tp}{}^1$ or additionally uses its bidentate N_{py},$N_{tp}{}^2$-coordination pocket. In $[Cu^{II}_2(\mu\text{-}\mathbf{L})_2(MeCN)_4](ClO_4)_4$·3.73MeCN·0.80$H_2O$ (**1**·3.73MeCN·0.80H_2O), only the second coordination mode is observed. The donor atoms involved in this coordination mode, $N_{tp}{}^2$, $N_{tp}{}^1$, and N_{py}, occupy the apexes and one equatorial position of a distorted trigonal bipyramid (**1**·3.73MeCN·0.80H_2O: τ = 0.76) or the apex and two *trans*-positions of the distorted square pyramid (**2**·solvent: τ = 0.15, 0.07, 0.07 for solvent = 2MeCN·2H_2O, 2MeCN·H_2O, and 1.5MeOH·3.5H_2O, respectively). The double-bridging coordination mode with a Cu···Cu separation of about 4 Å is a common structural feature of those complexes. Whereas in **1**·3.73MeCN·0.80H_2O the pyridyl and triazolopyridine ring are arranged

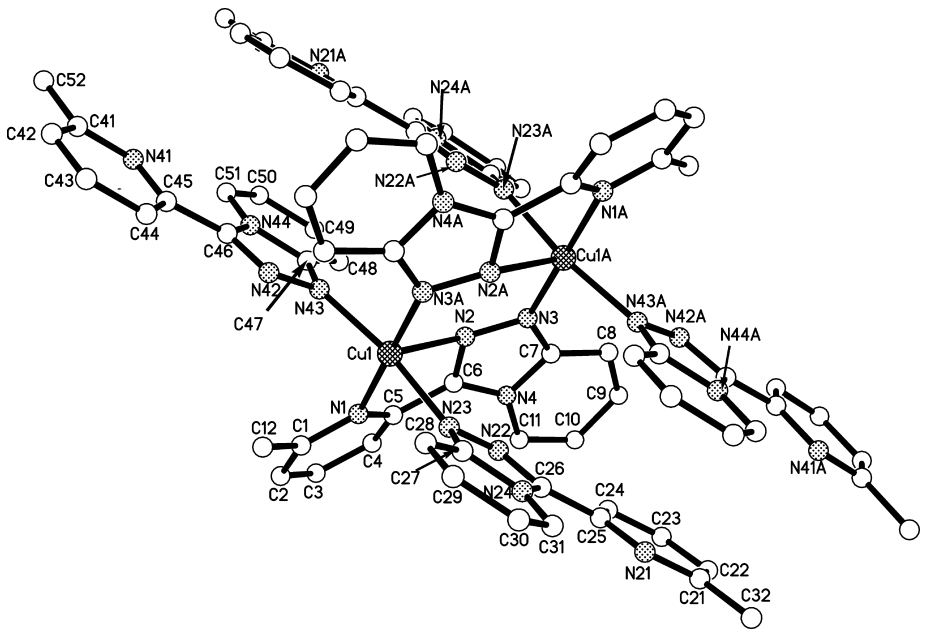

Figure 4. View of the molecular structure of $[Cu^{II}_2(\mathbf{L})_6]^{4+}$, the complex cation of (**2**·2MeCN·2H_2O). Hydrogen atoms are omitted for clarity. Symmetry operation used to generate equivalent atoms: (A) $-x, -y + 2, -z + 1$.

dx.doi.org/10.1021/ic500226z | *Inorg. Chem.* 2014, 53, 5546−5555

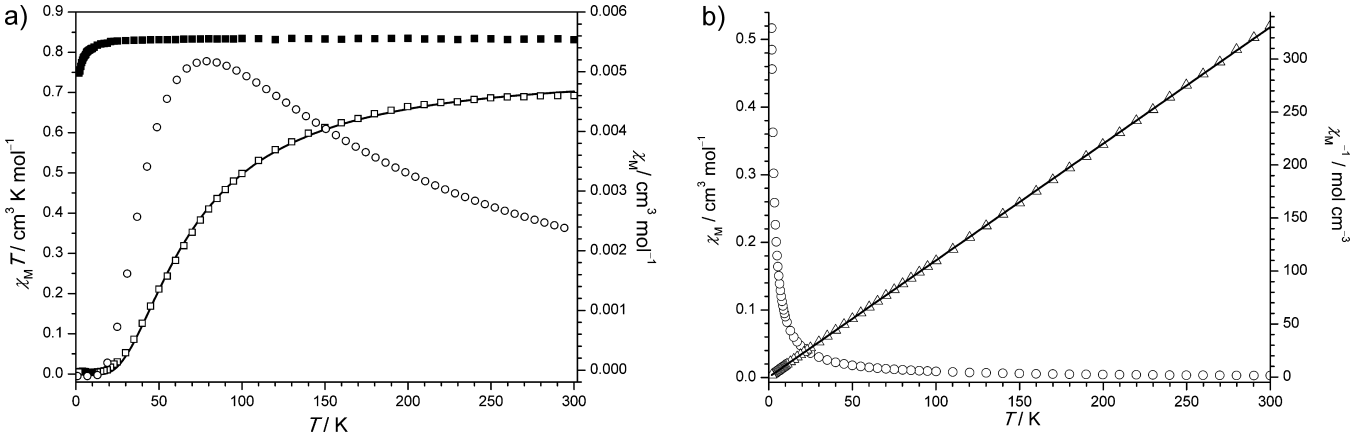

Figure 5. (a) Magnetic data for **1a** (open squares, □, $\chi_M T$ and open circles, ○, χ_M vs T) and **2**·2H_2O (full squares, ■, $\chi_M T$ vs T). (b) Magnetic data for **2**·2H_2O (open circles, ○, χ_M vs T and open triangles, △, χ_M^{-1} vs T). The solid line represents the fit as discussed in the main text.

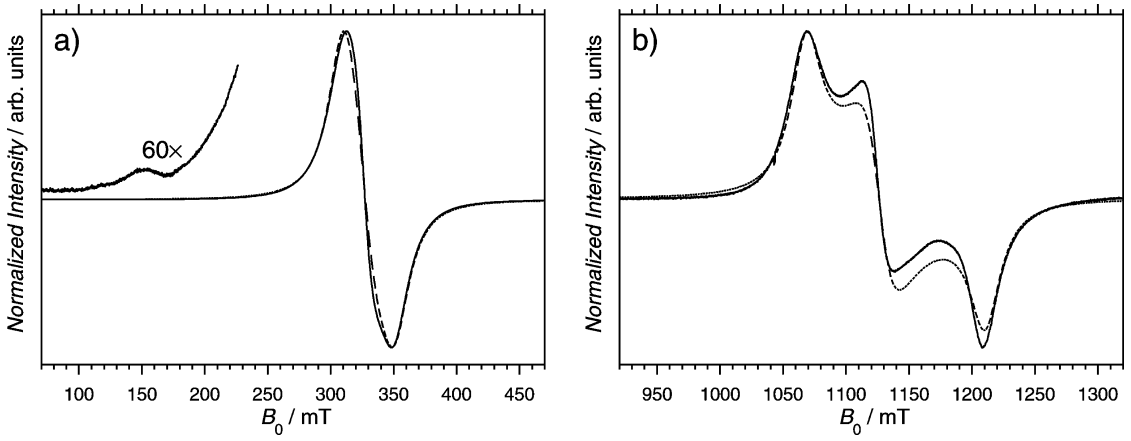

Figure 6. Continuous-wave EPR spectra of **1a** at (a) X-band (9.858 GHz) and (b) Q-band (34.025 GHz) at RT (solid lines) and simulated spectra using parameters as given in the main text (dashed lines). Part of the spectrum in (a) is magnified as indicated. Experimental conditions: (X-band) microwave power, 0.063 mW; magnetic field modulation amplitude, 0.1 mT (100 kHz modulation frequency); time-constant, 81.92 ms. (Q-band) microwave power, 7.24 mW; magnetic field modulation amplitude, 0.3 mT (100 kHz modulation frequency); time-constant, 40.96 ms.

relatively planar to each other and share an angle of 10.4(1)°, in **2**·solvent the respective rings are twisted a little further with angles of 28.8(1), 26.2(3), and 27.4(2)° for solvent being 2MeCN·2H_2O, 2MeCN·H_2O, and 1.5MeOH·3.5H_2O, respectively.

Similar dinuclear copper(II) complexes with doubly azole-bridged metal ions have been observed with the pyrazolate-based anionic ligands **A**, **B**, **C**, **E**, and **I** (Figure 1a)[4−8,13−15] and with the 1,2,4-triazole-based ligands **D**, **F**, and **G** (Figure 1a),[1,9−12] as well as with the ligand 6-methyl-3-pyridin-2-yl-7*H*-[1,2,4]triazolo[3,4-*b*][1,3,4]thiadiazine (**H**, Figure 1a).[9] Up until now, this coordination motif has not been observed for a tetracationic complex, as **1** and **2** features. Supporting Information, Tables S1 and S2 summarize the crystallographic data, selected bond distances, and angles of the new structures described in the text.

Magnetic Properties. The thermal variation of the molar magnetic susceptibilities (χ_M) of **1a** and **2**·2H_2O were measured over the range of 2−300 K with an applied magnetic field of 0.1 T (Figure 5a). Antiferromagnetic interaction of a moderate strength was identified in **1a**; however, unambiguous interpretation of the results for **2**·2H_2O was not possible. The χ_M vs T curve for complex **1a** was recorded with a maximum at about 80 K, indicating the presence of strong antiferromagnetic interactions. No such maximum was observed for complex **2**·2H_2O. The $\chi_M T$ value at 300 K for **1a** is equal to 0.7 cm^3 K mol^{-1}, slightly smaller than the spin-only value for the sum of two uncoupled electrons ($\chi_M T$ = 0.75 cm^3 K mol^{-1} for g = 2.0). For complex **2**·2H_2O this value is much higher at 300 K ($\chi_M T$ = 0.83 cm^3 K mol^{-1}) and stays at that value until very low temperatures of about 10 K, where it decreases rapidly. The $1/\chi_M$ vs T plot of complex **2**·2H_2O was fitted to the Curie−Weiss law $\chi_M = C/(T - \Theta)$ using the parameters C = 0.91 cm^3 K mol^{-1} and Θ = 0.06 K, indicating very weak magnetic coupling (Figure 5b). To estimate a magnitude of the magnetic exchange constant J between the copper(II) ions, the isotropic Heisenberg−Dirac−van Vleck Hamiltonian formalism was used.

$$\hat{H} = -J\hat{S}_1\hat{S}_2 \quad (1)$$

The magnetic data was analyzed using the Bleany−Bowers equation

$$\chi_M = \frac{2N_A g^2 \beta^2}{kT[3 + \exp(-J/kT)]} \quad (2)$$

where N_A, k, β, and g are the Avogadro number, the Boltzmann constant, the Bohr magneton, and the g-factor, respectively. The best fit to the experimental data of **1a** was obtained for J =

dx.doi.org/10.1021/ic500226z | Inorg. Chem. 2014, 53, 5546−5555

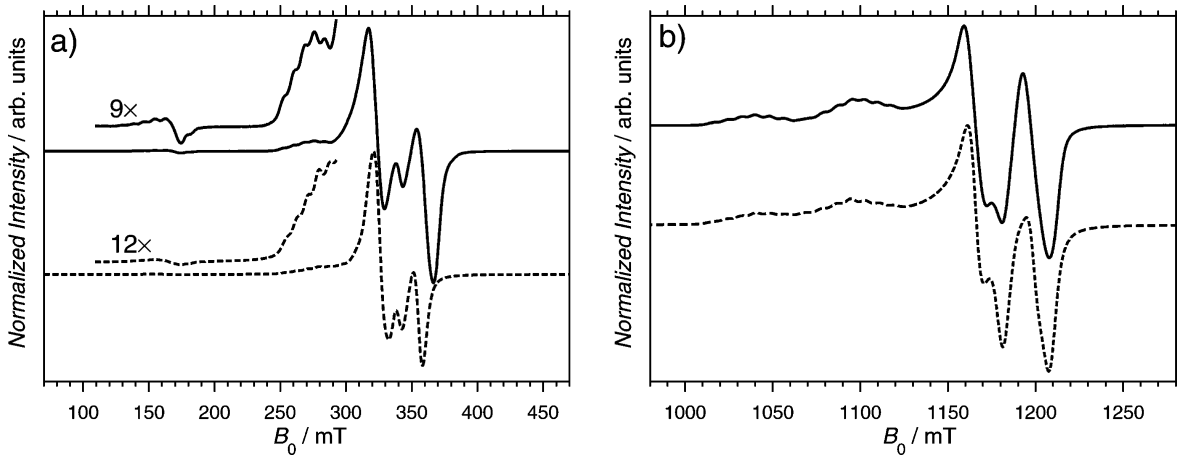

Figure 7. Cw-EPR spectra of **2**·2H_2O at (a) X-band (9.407 GHz) and (b) Q-band (34.095 GHz) at RT (solid lines) and simulated spectra using parameters as given in the main text (dashed lines). The very small signal around $g = 2$ was identified as a double-quantum transition and was added separately to the simulation.[26] Parts of the spectra in (a) are magnified as indicated. Experimental conditions: (X-band); microwave power, 0.063 mW; magnetic field modulation amplitude, 0.1 mT (100 kHz modulation frequency); time-constant, 40.96 ms. (Q-band) microwave power, 7.24 mW; magnetic field modulation amplitude, 0.3 mT (100 kHz modulation frequency); time-constant, 40.96 ms.

-87.8 cm^{-1}, $g = 2.10$, and $\chi_{dia} = -9.9 \times 10^{-5}$ cm^3 mol^{-1}. Because of a very weak copper(II)−copper(II) interaction in **2**·2H_2O an unambiguous fit of eq 2 to the experimental data was not possible. Field-dependent measurements of magnetization were performed for both compounds at 2 K. For **1a** the magnetization M only reaches about 0.02 μ_B at the highest field of 7 T, confirming the strong antiferromagnetic coupling (Figure S1a, Supporting Information). For compound **2**·2H_2O the magnetization M equals about 2.2 μ_B at 7 T, which is consistent with the presence of a very weak antiferromagnetic coupling, the strength of which is easily overcome by application of an external field allowing the magnetization to reach saturation of two isolated copper(II) ions (assuming $g = 2.2$). In conclusion, a rather strong antiferromagnetic interaction is observed for **1a**, whereas the antiferromagnetic interaction in **2**·2H_2O is only very weak, despite very similar molecular structures and Cu(II)···Cu(II) bridging motifs and distances.

EPR Spectroscopy. The room-temperature (RT) continuous-wave (cw) EPR spectra of a powdered sample of complex **1a** were recorded at both X-band (9.8 GHz) and Q-band (35.0 GHz) and are presented in Figure 6a, b, respectively. The X-band spectrum consists of a single broad line centered on $g = 2.15$. A very weak $\Delta M_S = 2$ transition is apparent only after magnification of the half-field region of the spectrum. Anisotropic components of the **g**-tensor were resolved in the Q-band spectrum; however, no $\Delta M_S = 2$ transition was observed.

Satisfactory, simultaneous simulations of the X- and Q-band spectra (Figure 6a and 6b) were obtained with a rhombic **g**-tensor ($g_z = 2.007$, $g_y = 2.157$, and $g_x = 2.278$) and a line width (full width at half height of the Lorentzian lines) $\Delta B = 17$ mT, indicating that the ground state arises from a combination of d_{z^2} and $d_{x^2-y^2}$ orbitals with a greater contribution from the d_{z^2} orbital, which is in agreement with $\tau = 0.76$ of the distorted trigonal bipyramidal coordination sphere (Figure 8, top).

The temperature dependence of all spectral features in the X-band EPR spectrum is shown in Figure S2a (Supporting Information). Typical features, characteristic for a triplet state, can only be observed upon cooling the sample from RT to 6 K. Increased resolution of the spectra at low temperatures is accompanied by decrease of intensity (Figure S2b, Supporting Information), indicating antiferromagnetic coupling between copper ions within a dimer and supporting the findings from the magnetic susceptibilities measurements. At 6 K both $\Delta M_S = 1$ and $\Delta M_S = 2$ transitions are present with an apparent splitting of the former signal due to the zero-field splitting. Also the copper hyperfine lines are clearly resolved in both the low-field part of $\Delta M_S = 1$ and $\Delta M_S = 2$ transitions. The integrated intensity of EPR signals for systems with thermally accessible triplet states depends on temperature as[25]

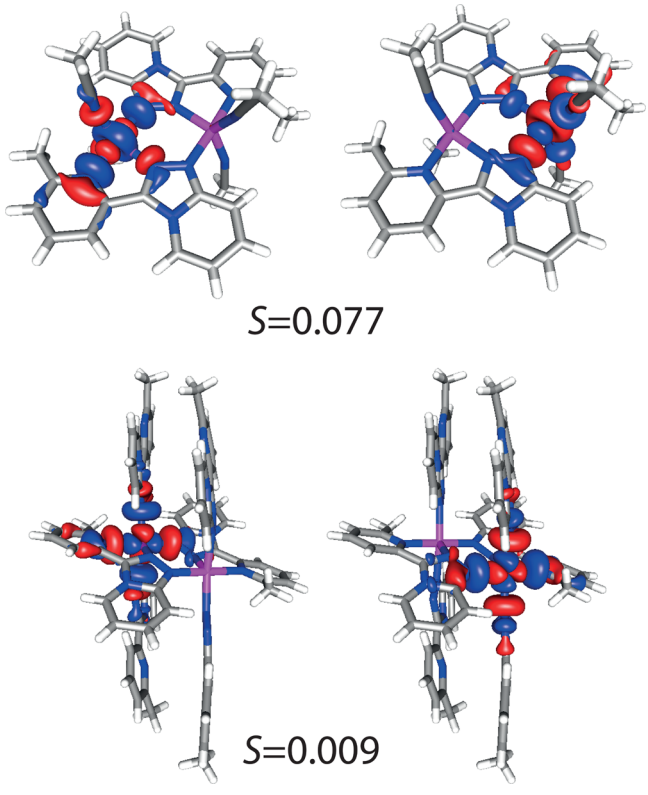

Figure 8. Magnetic orbitals of the molecular models based on crystallographic structures of **1**·3.73MeCN·0.80H_2O (top) and **2**·2H_2O (bottom).

dx.doi.org/10.1021/ic500226z | Inorg. Chem. 2014, 53, 5546−5555

$$T^{-1}[3 + \exp(-J/k_bT)]^{-1} \quad (3)$$

This relationship was employed to analyze the temperature dependence of the EPR signal. A value of $J = -100 \pm 7$ cm^{-1} was obtained from a least-squares fit of eq 3 to the experimental data (Figure S3, Supporting Information).

Cw-EPR measurements for a crystalline sample of complex **1**·3.73MeCN·0.80H_2O showed that, exposed to air, the compound is not stable over a longer period of time as changes in spectral shape were observed. After several days, the spectrum resembled that of the bulk compound **1a** (Figure S4, Supporting Information).

X-band and Q-band cw-EPR spectra were recorded for a powdered sample of **2**·2H_2O at various temperatures. The RT X-band spectrum (Figure 7a) reveals well-resolved characteristic features of a triplet-state with a high-field ($\Delta M_S = 1$) and a low-field ($\Delta M_S = 2$) transition. The signal for the $\Delta M_S = 2$ transition is relatively weak; however, it appears on the same scale as that for the transition $\Delta M_S = 1$. Clearly resolved copper hyperfine lines are present in the X-band spectrum on both the low-field edge of the $\Delta M_S = 1$ and the $\Delta M_S = 2$ transition (Figure 7a). A seven-line hyperfine splitting pattern with relative intensities of 1:2:3:4:3:2:1 is characteristic for two copper nuclei ($I = 3/2$) in a dimeric triplet state. Only the first five lines of the septet are apparent in the X-band spectrum, with the remaining two lines overlapping with the more intense signal of the $g_\perp$ component. Additional resolution of the $\Delta M_S = 1$ transition is provided by the Q-band measurement. Because of the low probability of the formally forbidden $\Delta M_S = 2$ transition at higher magnetic fields only a very weak signal was observed at Q-band (not shown). All seven lines of the hyperfine splitting are clearly visible in the $g_\parallel$ part of the spectrum (Figure 7b). From the simultaneous simulations of both X- and Q-band spectra the following spin Hamiltonian parameters were derived: $g_x = 2.058$, $g_y = 2.080$, $g_z = 2.303$, $A_z = 260$ MHz, $|D_S| = 0.0294$ cm^{-1}, and $|E_S| = 0.001$ cm^{-1}. The nearly axial character of the **g**-tensor with $g_z > g_x \approx g_y$ indicates that the ground state arises from a $d_{x^2-y^2}$ orbital, what is in agreement with $\tau = 0.07-0.15$ of the square pyramidal coordination sphere.

Cooling the sample to the temperature of 7 K did not change the resolution of the spectra, except for a slight broadening that is apparent at the lowest temperature (Figure S5a, Supporting Information). Moderate increase of intensity (Figure S5b, Supporting Information) follows the temperature dependence according to eq 3 supporting a very weak antiferromagnetic interaction between copper atoms. A value of $J = -9 \pm 2$ cm^{-1} was obtained from a least-squares fit of eq 3 to the experimental data (Figure S6, Supporting Information). The obtained value provides only the upper bound to the exact value, as within the available temperature range the maximum of the function was not observed.

DFT Calculation of Exchange Constants. The exchange coupling constant J was calculated for both complexes, **1a** and **2**·2H_2O, using the well-known broken-symmetry (BS) approach[27,28] in the context of density functional theory (DFT) as implemented in ORCA. In this BS-DFT formalism, applied to copper dimers, open-shell orbitals are localized on the two copper centers, and two subsequent calculations are carried out. In the first one, for high-spin state, all unpaired electrons are "spin up," while in the second calculation, for the BS spin state, the "spin up" open shell orbital is localized on one copper center, and the "spin-down" orbital is localized on the other one. Several schemes are known to map the energy difference between the high-spin and BS spin states to the one of the Heisenberg–Dirac–van Vleck Hamiltonian state.[27−32] In this Paper we will follow the formalism proposed by Yamaguchi and co-workers,[31,32] which is supposed to be independent of the bonding situation and applicable to any coupling strength. The crystallographic structure of **2**·2H_2O was used without further optimization. First, the molecular structure of **1**·3.73MeCN·0.80H_2O was used as a model structure for **1a**. Single crystals suitable for X-ray diffraction analysis could not be collected for **1a**, which is obtained as bulk material upon drying of **1**·3.73MeCN·0.80H_2O. Elemental analysis suggested that in the drying process exchange of MeCN coligands for water molecules occurs. We believe that the proposed exchange of the out-of-plane ligands for coligands of comparable size will have only a subordinate effect on the coupling strength. The effect of the coordination geometry about the copper(II) ions is assumed to be predominant and is not expected to change significantly, when substituting MeCN with H_2O; the case is quite different for the substitution of MeCN with the significantly bulkier ligand **L** like in **2**·2H_2O. To investigate these assumptions in detail, a model structure with H_2O molecules as coligands was prepared by replacement of the MeCN coligands in the model based on the crystallogtraphic structure of **1**·3.73MeCN·0.80H_2O. Subsequently, the geometry of the resulting model was either fully or partially optimized. In partially optimized structures the in-plane ligands **L** as well as the copper(II) ions were kept at their crystallographic positions, and only the geometries of the coligands were optimized.

Exchange coupling constants for all complexes were computed using the standard B3LYP hybrid functional, which is known to work very well within the BS-DFT framework (see, e.g., refs 33 and 34). The magnetic interactions within the systems are visualized by applying the corresponding orbital transformation to the BS solutions, where the spatial overlap S, associated with each pair of magnetic orbitals, indicates the strength of the interaction.[33]

The computed exchange coupling constants J for all the model structures of both **1** and **1a** vary between −154.44 and −210.46 cm^{-1} and are indicative of a strong antiferromagnetic interaction. All J values, computed for model structures, are summarized in Table S3 (Supporting Information). The smallest coupling constant was calculated for the model based on the crystallographic structure of **1**. Full optimization of the structure resulted in noticeable changes in the overall geometry of the complex (Figure S7, Supporting Information); however, the local geometry of the copper ions stayed the same and provided a nearly unchanged exchange coupling constant. Small increase of the interaction strength, of about 10 cm^{-1}, was calculated for the partially optimized structure, where only the coligand geometries have been relaxed. When H_2O was used as coligand, comparable values of exchange coupling constants J have been calculated for partially and fully optimized structures, equal to −200.26 and −210.46 cm^{-1}, respectively. Regardless of a rather small difference in the computed J values for both model structures of **1a**, nonnegligible differences in the local geometries of the copper(II) ions as well as in the geometries of the in-plane ligands were observed (Figure S8 and τ values in Table S3, Supporting Information). Elongation or shortening of the Cu–OH_2 bonds, mimicking the possible effects of crystal packing, resulted always in an increase or decrease, respectively, of the exchange interaction within the complex. Simultaneous

dx.doi.org/10.1021/ic500226z | Inorg. Chem. 2014, 53, 5546−5555

reoptimization of the structures, keeping the Cu−O bond lengths fixed, affected consistently the local geometries of the copper(II) ions. Increase of the bond lengths resulted in the increase of both the exchange coupling constant and the trigonal distortion parameter τ. Concluding, BS-DFT results for the model based on the crystallographic structure of **1**·3.73MeCN·0.80H_2O provide the smallest deviation from the experimental values. However, using either MeCN or H_2O as coligands, the divergence in the results is not large. Taking into account the intrinsic error of the BS-DFT calculations,[33] all computed exchange coupling constants for models of **1** and **1a** are in good agreement with experimetal findings, agreeing also with the assumption that the effect of coligand exchange for molecules of comparable size is small compared to the influence of the coordination geometry of copper(II). Inspection of the corresponding orbitals clearly shows the superexchange interaction to be mediated through the bonds of bridging atoms, with a spatial overlap of magnetic orbitals equal to S = 0.077 for the model based on the crystallographic structure (Figure 8, top).

The exchange coupling constant J = −1.82 cm^{-1} was calculated for **2**·2H_2O with a spatial overlap of magnetic orbitals S = 0.009 (Figure 8, bottom). Regardless of the nearly identical geometry of the bridging motifs in both complexes significant differences in the efficiency of superexchange pathways are observed. The main contributions to the magnetic orbitals, shown in Figure 8, can be easily identified as d_{z^2} and $d_{x^2-y^2}$ orbitals of copper(II) in **1** and **2**·2H_2O, respectively.

CONCLUSIONS

Coordination reactions with divalent 3d transition metal ions of the ligand 3-(6-methyl-2-pyridyl)-[1,2,4]triazolo[4,3-*a*]pyridine (**L**) differ significantly from those of the ligands 3-(2-pyridyl)-[1,2,4]triazolo[4,3-*a*]pyridine] ($\mathbf{L^1}$)[17] and 3-(2-pyrazyl)-[1,2,4]triazolo[4,3-*a*]pyridine ($\mathbf{L^2}$).[18] Whereas $\mathbf{L^1}$ and $\mathbf{L^2}$ readily form complexes with iron(II), cobalt(II), nickel(II), and copper(II), **L** readily forms complexes with copper(II) solely. It has also a strong preference to form dinuclear complexes with azole-bridged metal ions, which has been observed neither for $\mathbf{L^1}$ nor $\mathbf{L^2}$. This difference in coordination behavior is proposed to be due to sterical rather than electronic reasons.[18] The sole presence of the methyl group in **L** increases the sterical stress of the bidentate binding pocket in such a way that the bridging motif is preferred over the *trans-N,N′* coordination mode, as favored by $\mathbf{L^1}$. This finding also explains **L**'s preference for copper(II) over iron(II), cobalt(II), or nickel(II). Among those ions copper(II) has the strongest tolerance for five-coordinate architectures that are able to comply with this coordination motif. As a result **L** forms complexes with either a 3:1 (6:2) or a 1:1 (2:2) ratio but, unlike $\mathbf{L^1}$, not with a 2:1 ligand-to-metal ion stoichiometry. A predominantly trigonal bipyramidal coordination (τ = 0.76) is found in $[Cu^{II}_2(\mathbf{L})_2(MeCN)_4](ClO_4)_4$ (**1**), and the ligand's rings are almost in-plane. The magnetic orbitals arise from a combination of d_{z^2} and $d_{x^2-y^2}$ orbitals with a greater contribution from d_{z^2} orbital, and their overlap results in strong antiferromagnetically coupled copper(II) centers. A square pyramidal coordination (τ = 0.07−0.15) is observed in $[Cu^{II}_2(\mathbf{L})_6](ClO_4)_4$ (**2**), in which the magnetic $d_{x^2-y^2}$ orbitals are perpendicular to the Cu−(N−N)−Cu plane and sheared to each other allowing no efficient overlap. Here the ligand's rings are twisted slightly with respect to each other, which further hampers the exchange pathway. This is contrary to similar complexes published so far,[1,5,7,11] where the $d_{x^2-y^2}$ orbitals are in plane with the bridging motif. The strength of the antiferromagnetic coupling of diazine-bridged complexes therefore is not solely dependent on the symmetry of the bridge, but depends also strongly on the trigonal distortion parameter τ and thus the orientation of the magnetic orbitals. As a result the molecular structure of complex **2** provides no efficient path for exchange interactions, and only a very small antiferromagnetic J value was found.

EXPERIMENTAL SECTION

Materials. All starting materials and metal salts were purchased from commercial sources and were used as received. All solvents used were laboratory reagent grade. Manipulations were carried out in air.

Methods. Each melting point (mp) was determined using a Thiele mp apparatus. Elemental analyses were carried out using an Elementar Vario EL analyzer. IR spectra were recorded over the range of 4000−400 cm^{-1} using a Nicolet Magna 760 FTIR spectrometer. NMR spectra were recorded on a Bruker AVANCE II 400 WB spectrometer with a 5 mm ATM BBFO probe head, the decoupler coil tuned to the frequency of ^1H (400.17 MHz, 12 μs 90° pulse) and the detector coil tuned to the frequency of ^{13}C (100.62 MHz, 10.2 μs 90° pulse). ^1H and ^{13}C chemical shifts are given relative to tetramethylsilane using the residual solvent peak as the reference signal. Variable-temperature magnetic susceptibility measurements were carried out on microcrystalline, ground samples using a Quantum Design MPMSXL SQUID susceptometer over the range of 300−2 K (0.1 T) in both the cooling and heating mode. Magnetic data were corrected for sample holder and Pascal constants based on their ligand backbones. All X-band continuous-wave (cw) EPR data were obtained using a Bruker Elexsys E680 spectrometer equipped with a Bruker ER 4118X-MD5 resonator. For cooling an Oxford CF-935 cryostat was used. The temperature was regulated by a temperature controller (Oxford ITC-503). The Q-band cw-EPR data were obtained using a Bruker ESP 380E spectrometer equipped with a Bruker ER 5106QT-W1 resonator. For cooling, an Oxford CF-935 cryostat and an Oxford ITC-4 temperature controller were used. The samples were filled into synthetic silica glass tubes of ∼1.6 mm outer diameter for both X-band and Q-band measurements. All EPR spectra were analyzed and simulated using EasySpin.[35] Single-crystal X-ray diffraction data were collected using a Bruker APEX-II CCD diffractometer with a microfused sealed tube radiation source, using graphite-monochromated Mo Kα radiation (λ = 0.710 73 Å). The structures were solved by direct methods with SHELXS-97[36] and refined against F^2 using all data by full-matrix least-squares techniques with SHELXL-97.[36] All non-hydrogen atoms were refined anisotropically, except for the solvent molecules in **2**·2MeCN·H_2O and the disordered ClO_4^- anions in **2**·2MeCN·2H_2O. All hydrogen atoms were placed at calculated positions using riding models. In complex **1**·3.73MeCN·0.80H_2O the partially occupied MeCN solvate (occupancy factor 0.866) shares its approximate position with three partially occupied H_2O molecules (occupancy factors 0.133). Broken-symmetry DFT calculations of exchange coupling constants J were performed with ORCA program package[37] using the B3LYP[38−40] functional. Def2-TZVPP[41−43] basis functions were used for Cu and N atoms. Def2-SVP[41] basis functions were used for C and H atoms. Increased integration grid (Grid5 in ORCA nomenclature) and very tight SCF convergence criteria were used. The resolution of the identity together with "chain of spheres"[44] approximations (RIJCOSX) were used. Structural models based on crystallographic structures were used either with or without further optimization. All structure optimizations were carried out with the ORCA program package[37] using the BP86 functional[45,46] and Def2-TZVPP[41−43] basis functions for Cu, N and O atoms and Def2-SVP[41] basis functions for C and H atoms. In this Paper we discuss the computed J values following the formalism proposed by Yamaguchi and co-workers,[31,32] which is supposed to be independent of the bonding situation and applicable to any coupling strength.

dx.doi.org/10.1021/ic500226z | Inorg. Chem. 2014, 53, 5546−5555

*N-(2-Pyridylamino)-2-(6-methylpyridine)amidine (**J**).* The following reaction was performed under a protective argon atmosphere in a sealed vessel, completely wrapped in tinfoil. A solid mixture of 6-methyl-2-cyanopyridine (2.13 g, 18.0 mmol) and 2-pyridylhydrazine (1.97 g, 18.0 mmol) was kept at 80−85 °C for a week. Recrystallization from EtOAc/cyclohexane (1:1) gave a crystalline mixture of **J** and **L**, which was used as such for further reactions. ^{1}H NMR (200.13 MHz, $CDCl_3$): δ = 8.14 (ddd, $^3J_{5,6}$ = 5.0 Hz, $^4J_{4,6}$ = 1.8 Hz, $^5J_{3,6}$ = 1.0 Hz, 1 H, 6-Py*H*), 8.04 (ddd, $^3J_{3,4}$ = 8.0 Hz, $^4J_{3,5}$ = 0.9 Hz, *J* = 0.5 Hz, 1 H, 3-^{Me}Py*H*), 7.62 (t,$^3J_{3,4}$(^{Me}Py) = $^3J_{3,4}$(Py) = $^3J_{4,5}$ = 8.0 Hz, 2 H, 4-^{Me}Py*H* + 4-Py*H*), 7.31 (dt, $^3J_{3,4}$ = 8 Hz, $^4J_{3,5}$ = $^5J_{3,6}$ = 1.0 Hz, 1 H, 3-Py*H*), 7.15 (ddd, $^3J_{4,5}$ = 8.0 Hz, $^4J_{3,5}$ = 1 Hz, *J* = 0.5 Hz, 1 H, 5-^{Me}Py*H*), 6.76 (ddd, $^3J_{4,5}$ = 8 Hz, $^3J_{5,6}$ = 5 Hz, $^4J_{3,5}$ = 1 Hz, 1 H, 5-Py*H*), 5.51 (s, 2 H, NH_2), 2.57 (s, 3 H, CH_3) ppm. ^{13}C NMR (100.62 MHz, CD_3Cl): δ = 158.2 (2-PyC), 156.5 (6-^{Me}PyC), 150.8 (2-^{Me}PyC), 147.8 (6-PyC), 141.3 (NCNH$_2$), 137.9 (4-PyC), 137.1 (4-^{Me}PyC), 123.0 (5-^{Me}PyC), 117.1 (3-^{Me}PyC), 114.1 (5-PyC), 106.4 (3-PyC), 24.4 (CH_3) ppm.

*3-(6-Methyl-2-pyridyl)-[1,2,4]triazolo[4,3-a]pyridine (**L**).* A mixture of crude products **J** and **L**, produced from 6-methyl-2-cyanopyridine (3.52 g, 29.8 mmol) and 2-pyridylhydrazine (3.25 g, 29.8 mmol), was heated in acetic acid (15 mL) to reflux for 5 h. After removal of all volatiles *in vacuo*, the residue was recrystallized from EtOAc/cyclohexane (1:1, 80 mL) to afford analytically pure **L** (2.25 g, 36%) in the form of a crystalline solid. Single crystals suitable for X-ray diffraction were obtained by this method. Elemental analysis (%) found: C 68.54, H 4.68, N 26.56; calcd. for $C_{12}H_{10}N_4$ (210.24 g mol^{-1}): C 68.56, H 4.79, N 26.65. mp = 158 °C. ^{1}H NMR (200.13 MHz, $CDCl_3$): δ = 9.87 (dt, $^3J_{5,6}$ = 7.1 Hz, $^4J_{5,7}$ = $^5J_{5,8}$ = 1.2 Hz, 1 H, 5-Tp*H*), 8.34 (ddd, $^3J_{3,4}$ = 7.8 Hz, $^4J_{3,5}$ = 0.9 Hz, *J* = 0.5 Hz, 1 H, 3-Py*H*), 7.86 (dt, $^3J_{7,8}$ = 9.3 Hz, $^4J_{6,8}$ = $^5J_{5,8}$ = 1.2 Hz, 1 H, 8-Tp*H*), 7.76 (t, $^3J_{3,4}$ = $^3J_{4,5}$ = 7.8 Hz, 1 H, 4-Py*H*), 7.35 (ddd, $^3J_{7,8}$ = 9.3 Hz, $^3J_{6,7}$ = 6.6 Hz, $^4J_{5,7}$ = 1.2 Hz, 1 H, 7-Tp*H*), 7.21 (ddd, $^3J_{4,5}$ = 7.8 Hz, $^4J_{3,5}$ = 0.9 Hz, *J* = 0.5 Hz, 1 H, 5-Py*H*), 6.96 (ddd, $^3J_{5,6}$ = 7.1 Hz, $^3J_{6,7}$ = 6.6 Hz, $^4J_{6,8}$ = 1.2 Hz, 1 H, 6-Tp*H*), 2.66 (s, 3 H, CH_3) ppm. ^{13}C NMR (100.62 MHz, $CDCl_3$): δ = 157.5 (6-PyC), 151.1 (9-TpC), 147.2 (2-PyC), 144.3 (3-TpC), 137.3 (4-PyC), 127.6 (7-TpC), 127.3 (5-TpC), 123.2 (5-PyC), 119.6 (3-PyC), 115.9 (8-TpC), 113.8 (6-TpC), 24.2 (CH_3) ppm. IR (diamond ATR): $\tilde{\nu}$ = 1630.9, 1590.8, 1579.6, 1494.7 (s), 1450.0, 1364.5, 1320.1, 1157.0, 1137.3, 1085.6 (s), 1039.5, 1002.0, 861.4, 793.7, 773.0 (s), 729.1, 697.3, 684.2, 631.7, 551.8, 512.5, 425.0 cm^{-1}.

***Caution!** While no problems were encountered in the course of this work, ClO_4^- salts are potentially explosive and should be handled with appropriate care.*

*[Cu$^{II}_2$(**L**)$_2$(MeCN)$_4$](ClO$_4$)$_4$ (**1**).* A solution of Cu(ClO$_4$)$_2$·6H$_2$O (111.2 mg, 300 μmol) in MeCN (20 mL) was added to a solution of **L** (63.1 mg, 300 μmol) in MeCN (50 mL). Vapor diffusion of TBME into the dark green reaction solution resulted in the formation of a green crystalline solid, which was identified by X-ray diffraction as complex **1**·3.73MeCN·0.80H$_2$O. Filtration and drying in air gave bulk material of [Cu$^{II}_2$(**L**)$_2$(H$_2$O)$_4$](ClO$_4$)$_4$ (**1a**). Yield: 49%. mp > 240 °C. Elemental analysis (%) found: C 28.67, H 3.17, N 11.48; calcd. for $C_{24}H_{28}N_8O_{20}Cl_4Cu_2$ (1017.43 g mol^{-1}): C 28.33, H 2.77, N 11.01. IR (diamond ATR): $\tilde{\nu}$ = 3372.4 (b), 1643.6, 1620.8, 1523.3, 1460.8, 1437.5, 1049.8 (vs, b), 927.6, 792.5, 753.8, 735.2, 704.8, 691.8, 619.9 (s), 576.1, 424.3 cm^{-1}.

*[Cu$^{II}_2$(**L**)$_6$](ClO$_4$)$_4$ (**2**).* (a) From MeCN with TBME: A solution of Cu(ClO$_4$)$_2$·6H$_2$O (74.1 mg, 200 μmol) in MeCN (5 mL) was added to a solution of **L** (126.1 mg, 600 μmol) in MeCN (10 mL). Vapor diffusion of TBME into the dark green reaction solution resulted in the formation of a dark red-brown crystalline solid identified as [Cu$^{II}_2$(**L**)$_6$](ClO$_4$)$_4$·2MeCN·2H$_2$O (**2**·2MeCN·2H$_2$O) by single-crystal X-ray diffraction. Filtration and drying *in vacuo* gave bulk material of complex **2**·2H$_2$O. Yield: 82%. Elemental analysis (%) found: C 47,78, H 3.33, N 18.75; calcd. for $C_{72}H_{64}N_{24}O_{18}Cl_4Cu_2$ (1822.35 g mol^{-1}): C 47.45, H 3.54, N 18.45.

(b) From MeCN with Et$_2$O: A solution of Cu(ClO$_4$)$_2$·6H$_2$O (74.1 mg, 200 μmol) in MeCN (5 mL) was added to a solution of **L** (126.1 mg, 600 μmol) in MeCN (10 mL). Vapor diffusion of Et$_2$O into the dark green reaction solution resulted in the formation of a dark red-brown crystalline solid, which was identified by X-ray diffraction as complex **2**·2MeCN·H$_2$O. Filtration and drying *in vacuo* gave bulk material of complex **2**·2H$_2$O. Yield: 59%. Mp > 240 °C. Elemental analysis (%) found: C 46.98, H 3.42, N 18.51; calcd. for $C_{72}H_{64}N_{24}O_{18}Cl_4Cu_2$ (1822.35 g mol^{-1}): C 47.45, H 3.54, N 18.45. IR (diamond ATR): $\tilde{\nu}$ = 3620.4, 3547.3, 3120.5, 1637.5, 1576.8, 1500.3, 1457.1, 1074.2 (vs), 798.2, 760.9, 733.6, 697.5, 687.1, 620.4 (s), 557.4, 428.4 cm^{-1}.

(c) From MeOH: A solution of Cu(ClO$_4$)$_2$·6H$_2$O (18.5 mg, 50 μmol) in MeOH (5 mL) was added to a solution of **L** (31.5 mg, 150 μmol) in MeOH (20 mL), which resulted in a green reaction solution. Slow evaporation of the solvent resulted in the formation of a dark red-brown crystalline solid, which was identified by X-ray diffraction as complex **2**·1.5MeOH·3.5H$_2$O. Filtration and drying *in vacuo* gave bulk material of complex **2**·2H$_2$O. Yield: 55%. Elemental analysis (%) found: C 47.82, H 3.345, N 18.55; calcd. for $C_{72}H_{64}N_{24}O_{18}Cl_4Cu_2$ (1822.35 g mol^{-1}): 47.45, H 3.54, N 18.45.

■ ASSOCIATED CONTENT

Ⓢ Supporting Information

Crystallographic data for **L**, **1**·3.73MeCN·0.80H$_2$O, **2**·MeCN·2H$_2$O, **2**·2MeCN·H$_2$O, **2**·1.5MeOH·3.5H$_2$O (Table S1); selected distances and angles of the coordination environments of the complexes (Table S2); exchange coupling constants *J*, spatial overlap *S*, and trigonal distortion parameter τ for various model structures of **1** (**1**·3.73MeCN·0.80H$_2$O) and **1a** (Table S3); *M* vs *H* plots of **1a** and **2**·2H$_2$O at 2 K (Figure S1); temperature-dependent EPR spectra (X-band) of **1a** and **2**·2H$_2$O (Figure S2 and S5, respectively); temperature variation of the normalized integrated intensities of the EPR spectra at X-band for **1a** and **2**·2H$_2$O (Figures S3 and S6, respectively); EPR spectra of crystalline sample of **1**·3.73MeCN·0.80H$_2$O, freshly prepared and after several days (Figure S4); comparison of the partially and fully optimized model structures of **1** (Figure S7) and of the partially and fully optimized structures of **1a** (Figure S8); crystallographic data in CIF format. This material is available free of charge via the Internet at http://pubs.acs.org. CCDC 908449, 908451−908454 contain the supplementary crystallographic data for **L**, **2**·2MeCN·2H$_2$O, **1**·3.73MeCN·0.80H$_2$O, **2**·2MeCN·H$_2$O, and **2**·1.5MeOH·3.5H$_2$O, respectively. These data can be obtained free of charge at www.ccdc.cam.ac.uk/data_request/cif or from the Cambridge Crystallographic Data Centre, 12 Union Road, Cambridge CB2 1EZ, U.K.

■ AUTHOR INFORMATION

Corresponding Authors

*E-mail: julia.klingele@ac.uni-freiburg.de. Phone: +49-(0)761-203-6135. Fax: +49-(0)761-203-6001. (J.K.)

*E-mail: sylwia.kacprzak@physchem.uni-freiburg.de. Phone: +49-(0)761-203-6207. Fax: +49-(0)761-203-6222. (S.K.)

Notes

The authors declare no competing financial interest.

■ ACKNOWLEDGMENTS

We thank Prof. Oliver Waldmann for helpful discussions. Prof. Peter Roesky and Prof. Annie K. Powell are thanked for the allocation of technical equipment; Sabine Lude and Maximilian Schmucker are thanked for technical assistance. This project is supported by the European Social Fund and by the Ministry Of Science, Research, and the Arts Baden-Württemberg within the *Margarete von Wrangell Program*. J.K. is indebted to the Baden-Württemberg Stiftung for the financial support of this research project by the Eliteprogramme for postdoctoral students.

Financial support from the *Fonds der Chemischen Industrie* (FCI) is gratefully acknowledged. J.K. thanks Prof. Ingo Krossing and Prof. Harald Hillebrecht for their generous and continuous support. Y.L. is grateful to Prof. Annie K. Powell for her generous support. S.K. gratefully acknowledges Prof. Dr. Stefan Weber for valuable discussions and continuous support.

REFERENCES

(1) Slangen, P. M.; Koningsbruggen, P. J. v.; Goubitz, K.; Haasnoot, J. G.; Reedijk, J. *Inorg. Chem.* **1994**, *33*, 1121−1126.
(2) Tandon, S. S.; Thompson, L. K.; Hynes, R. C. *Inorg. Chem.* **1992**, *31*, 2210−2214.
(3) Melník, M. *Coord. Chem. Rev.* **1982**, *42*, 259−293.
(4) Jones, L. F.; Camm, K. D.; Kilner, C. A.; Halcrow, M. A. *CrystEngComm* **2006**, *8*, 719−721.
(5) Mokuolu, Q. F.; Foguet-Albiol, D.; Jones, L. F.; Wolowska, J.; Kowalczyk, R. M.; Kilner, C. A.; Christou, G.; McGowan, P. C.; Halcrow, M. A. *Dalton Trans.* **2007**, 1392−1399.
(6) Hallam, M. J.; Kilner, C. A.; Halcrow, M. A. *Acta Crystallogr.* **2002**, *C58*, m445−m446.
(7) Hu, T.-L.; Li, J.-R.; Liu, C.-S.; Shi, X.-S.; Zhou, J.-N.; Bu, X.-H.; Ribas, J. *Inorg. Chem.* **2006**, *45*, 162−173.
(8) Singh, K.; Long, J. R.; Stavropoulos, P. *Inorg. Chem.* **1998**, *37*, 1073−1079.
(9) Tardito, S.; Bussolati, O.; Maffini, M.; Tegoni, M.; Giannetto, M.; Dall'Asta, V.; Franchi-Gazzola, R.; Lanfranchi, M.; Pellinghelli, M. A.; Mucchino, C.; Mori, G.; Marchio, L. *J. Med. Chem.* **2007**, *50*, 1916−1924.
(10) Li, W.; Zhang, J.; Li, C.; Yang, Y. *Z. Kristallogr.* **2010**, *225*, 181−182.
(11) Wang, Z.-X.; Xu, H.-J.; Gong, X.-N.; Wu, P.-F. *Wuji Huaxue Xuebao* **2009**, *25*, 1492−1496.
(12) Wang, Z.; Liu, C.; Zhang, X.; Gong, X. *Acta Crystallogr.* **2007**, *E65*, m22−m22.
(13) Pons, J.; López, X.; Casabó, J.; Teixidor, F.; Caubet, A.; Rius, J.; Miravitlles, C. *Inorg. Chim. Acta* **1992**, *195*, 61−66.
(14) Munakata, M.; Wu, L. P.; Yamamoto, M.; Kuroda-Sowa, T.; Maekawa, M.; Kawata, S.; Kitagawa, S. *J. Chem. Soc., Dalton Trans.* **1995**, 4099−4106.
(15) Du, M.; Chen, S.-T.; Guo, Y.-M.; Bu, X.-H.; Ribas, J. *J. Mol. Struct.* **2005**, *737*, 17−21.
(16) Addison, A. W.; Rao, T. N.; Reedijk, J.; Rijn, J. v.; Verschoor, G. C. *J. Chem. Soc., Dalton Trans.* **1984**, 1349−1356.
(17) Klingele, J.; Kaase, D.; Hilgert, J.; Steinfeld, G.; Klingele, M. H.; Lach, J. *Dalton Trans.* **2010**, *39*, 4495−4507.
(18) Klingele, J.; Kaase, D.; Huxel, T.; Gotzmann, C.; Lan, Y. *Polyhedron* **2013**, *52*, 500−514.
(19) Kitchen, J. A.; Brooker, S. *Coord. Chem. Rev.* **2008**, *252*, 2072−2092.
(20) Klingele, M. H.; Brooker, S. *Coord. Chem. Rev.* **2003**, *241*, 119−132.
(21) Klingele, J.; Kaase, D.; Klingele, M. H.; Lach, J.; Demeshko, S. *Dalton Trans.* **2010**, *39*, 1689−1691.
(22) Klingele, J.; Kaase, D.; Klingele, M. H.; Lach, J. *Dalton Trans.* **2012**, *41*, 1397−1406.
(23) Klingele, J.; Kaase, D.; Schmucker, M.; Meier, L. *Eur. J. Inorg. Chem.* **2013**, 4931−4939.
(24) Klingele, J.; Kaase, D.; Schmucker, M.; Chastanet, G.; Létard, J.-F. *Inorg. Chem.* **2013**, *52*, 6000−6010.
(25) Weil, J. A.; Bolton, J. R. *Electron paramagnetic resonance: elementary theory and practical applications,* 2nd ed.; John Wiley & Sons, Inc.: Hoboken, NJ, 2007.
(26) Napolitano, L. M. B.; Nascimento, O. R.; Cabaleiro, S.; Castro, J.; Calvo, R. *Phys. Rev. B* **2008**, *77*, 214423.
(27) Noodleman, L. *J. Chem. Phys.* **1981**, *74*, 5737−5743.
(28) Noodleman, L.; Davidson, E. R. *Chem. Phys.* **1986**, *109*, 131−143.
(29) Ginsberg, A. P. *J. Am. Chem. Soc.* **1980**, *102*, 111−117.
(30) Ruiz, E.; Cano, J.; Alvarez, S.; Alemany, P. *J. Comput. Chem.* **1999**, *20*, 1391−1400.
(31) Yamaguchi, K.; Takahara, Y.; Fueno, T. *Applied Quantum Chemistry;* Smith, V. H., Ed.; Reidel: Dordrecht, Netherlands, 1986; pp 155.
(32) Soda, T.; Kitagawa, Y.; Onishi, T.; Takano, Y.; Shigeta, Y.; Nagao, H.; Yoshioka, Y.; Yamaguchi, K. *Chem. Phys. Lett.* **2000**, *319*, 223−230.
(33) Moreira, I. P. R.; Costa, R.; Filatov, M.; Illas, F. *J. Chem. Theory Comput.* **2007**, *3*, 764−774.
(34) Neese, F. *Coord. Chem. Rev.* **2009**, *253*, 526−563.
(35) Stoll, S.; Schweiger, A. *J. Magn. Reson.* **2006**, *178*, 42−55.
(36) Sheldrick, G. M. *Acta Crystallogr., Sect. A* **2008**, *64*, 112−122.
(37) Neese, F.*ORCA,* An ab initio, DFT and semiempirical electronic structure package, Version 2.9; Max-Planck-Institut für Bioanorganische Chemie: Mülheim, Germany, 2012.
(38) Lee, C.; Yang, W.; Parr, R. G. *Phys. Rev. B* **1988**, *37*, 785−789.
(39) Becke, A. D. *J. Chem. Soc., Chem. Commun.* **1993**, *98*, 5648−5652.
(40) Miehlich, B.; Savin, A.; Stoll, H.; Preuss, H. *Chem. Phys. Lett.* **1989**, *157*, 200−206.
(41) Schäfer, A.; Horn, H.; Ahlrichs, R. *J. Chem. Phys.* **1992**, *97*, 2571−2577.
(42) Weigend, F.; Ahlrichs, R. *Phys. Chem. Chem. Phys.* **2005**, *7*, 3297−3305.
(43) Weigend, F.; Häser, M.; Patzelt, H.; Ahlrichs, R. *Chem. Phys. Lett.* **1998**, *294*, 143−152.
(44) Neese, F.; Wennmohs, F.; Hansen, A.; Becker, U. *Chem. Phys.* **2009**, *356*, 98−109.
(45) Becke, A. D. *Phys. Rev. A* **1988**, *38*, 3098−3100.
(46) Perdew, J. P. *Phys. Rev. B* **1986**, *33*, 8822−8824. erratum: Perdew, J. P. *Phys. Rev. B* **1986**, *34*, 7406−7406.